Accurate modeling of the dynamics of dissociative chemisorption on metal surfaces

Gerrits, N.

Chapter 8

A High-Dimensional Neural Network Potential for the dissociative chemisorption of CHD_3 + Cu(111)

This chapter is based on Gerrits, N.; Shakouri, K.; Behler, J.; Kroes, G.-J. Accurate Probabilities for Highly Activated Reaction of Polyatomic Molecules on Surfaces Using a High-Dimensional Neural Network Potential: CHD_3 + Cu(111). *J. Phys. Chem. Lett.* **2019**, *10*, 1763–1768, DOI: 10.1021/acs.jpclett.9b00560

Abstract

An accurate description of reactive scattering of molecules on metal surfaces often requires the modeling of energy transfer between the molecule and the surface phonons. Although Born-Oppenheimer molecular dynamics (BOMD) can describe this energy transfer, BOMD is at present untractable for reactions with reaction probabilities smaller than 1%. Here, it is shown that it is possible to use a neural network potential to describe a polyatomic molecule reacting on a mobile metal surface, with considerably reduced computational effort compared to BOMD. The highly activated reaction of CHD_3 on Cu(111) is used as a test case for this method. It is observed that the reaction probability is influenced considerably by dynamical effects such as the bobsled effect and surface recoil. A special dynamical effect for CHD_3 + Cu(111) is that a higher vibrational efficacy is obtained for two quanta in the CH stretch mode than for a single quantum.

8.1 Introduction

Accurately describing molecule-metal surface reactions is of vital importance for the understanding of heterogeneously catalyzed processes such as the Haber-Bosch[1] and steam reforming processes[2]. Unfortunately, the complexity of the interaction between molecules and metals limits the accuracy of theoretical studies on these kinds of processes[3–8]. Often, chemically accurate results are obtainable at high computational cost with Born-Oppenheimer molecular dynamics (BOMD) combined with the so-called Specific Reaction Parameter (SRP) approach[9–11]. However, the investigation of reactions with low reactivity ($< 1\%$) remains challenging due to the need for a large number of trajectories in combination with a large computational cost[12]. Therefore, neural network approaches have recently been employed in order to obtain results with the accuracy of BOMD using density functional theory (DFT), but with a considerably smaller computational cost[13–16]. So far these studies involved either diatomic molecules[13–16], or they neglected the movement of surface atoms[17–21]. Very recently, a high-dimensional neural network potential (HD-NNP) has been developed for a system in which a linear triatomic molecule interacts with a metal surface, i.e., CO_2 + Ni(100)[22], while also including surface atom motion. The neglect of surface motion can limit the accuracy of these studies due to the neglect of energy exchange between the molecule and the surface atoms[4, 12, 15, 16, 23–28]. This lack of energy exchange represents a severe approximation for the dynamics of polyatomic molecules reacting on metal surfaces due to their high mass[29, 30]. A modified Shepard interpolation method[31] has also been used to describe the potential of a polyatomic molecule reacting on a metal surface, but again with the neglect of surface motion. Reactive force field fits have been made that do include surface motion[32–35]. Although Busnengo and coworkers have shown that these fits can be in good agreement with DFT[35], it remains unclear whether these fits are also chemically accurate, i.e., whether the root-mean-square error (RMSE) is lower than 4.2 kJ/mol for the dynamically relevant part of the potential energy surface (PES). However, at the time this work was performed, no neural network potential had been employed for non-linear polyatomic molecules interacting with metal surfaces that explicitly includes the effect of surface motion as well.

In this chapter, the focus is on the dissociative chemisorption of CHD_3 on Cu(111) since this system exhibits a low reactivity[12], making reactive BOMD studies untractable for most incidence energies achievable in molecular beams. Moreover, high-quality graphene can be synthesized using methane dissociation on copper[36–42], and this warrants additional study of the rate-

controlling state, namely the breaking of the first CH bond. The Eley-Rideal reaction of D with CD_3 preadsorbed on Cu(111) has also been studied[43]. The methane + Cu(111) system shows interesting dynamics in that the low reactivity of methane on Cu(111) is not only caused by a high barrier (167 kJ/mol), but also by specific features of the PES such as the curvature of the minimum energy path (MEP)[12] (see Chapter 7). For all of these reasons, the neural network Behler-Parrinello approach[44, 45] has been applied for the first time to a non-linear polyatomic molecule reacting on a metal surface, which makes accurate simulations feasible while including surface motion, using CHD_3 + Cu(111) as an example.

8.2 Method

8.2.1 Neural Network

In the HD-NNP, the total energy is evaluated as a sum of atomic contributions that are dependent on their energetically relevant local environment, which is described by many-body atom-centered symmetry functions[46] (see Section 2.3.2), of which the parameters are given in Section 8.A. In total, 38 000 DFT data points were used to train the HD-NNP, of which 14 000 points were taken from the BOMD study of Chapter 7. Points from the BOMD data set were selected with the following procedure. All reacted and 50 scattered trajectories were used from the BOMD study in Chapter 7, of which only 10% of the steps in the trajectories have initially been selected. From those selected steps, it is made sure that the methane geometry in a selected step is not too similar to other previously selected steps. The acceptance criterium for this selection is $\epsilon_{\text{min}} = 0.2$ Å, where

$$\epsilon_j > \epsilon_{\text{min}} \quad \text{for } j = 1, \ldots, N \tag{8.1}$$

$$\epsilon_j = \sqrt{\sum_i r_{i,j}^2}. \tag{8.2}$$

The atoms of the methane molecule are indicated by i, all previous geometries are indicated by j, and $r_{i,j}$ is the distance between atom i of the newly selected geometry and atom j of a previous methane geometry j. This procedure resulted in about 14 000 points in the training data set. Missing structures in the training data set (about 21 500) were found by running MD on the incomplete HD-NNP using the following procedure[45]. About 5000 trajectories were calculated at $\langle E_{\text{i}} \rangle = 160$ and 181 kJ/mol for laser-off conditions and $v_1 = 2$. The neural network implementation would then identify extrapolation errors during the MD, indicating structures that are missing in the training set. These

missing structures were then added to the training set and this procedure was repeated until the amount of extrapolation errors was considered small enough ($< 0.5\%$) and no longer affected the computed reaction probability. During the process of identifying missing structures, about 20 points in the Van der Waals well region were included as well. Also, 500 points from the elbow plot showing the minimum barrier (see Chapter 7), and where all degrees of freedom other than the molecule-surface distance Z and the length of the dissociating CH-bond r are relaxed, were included (see Figure 8.3c). Finally, vibrational modes were sampled in a random fashion according to a nozzle temperature of 1200 K, on both an ideal and thermally distorted surface (but note that the ideal surface still includes a lattice expansion corresponding to the simulated surface temperature of 550 K) at random locations with respect to the surface, resulting in 2000 points. Using the aforementioned procedures a total number of 38 000 of points were obtained that formed the training and testing data set. The total energy for all structures in the training and testing data set obtained with both DFT and the HD-NNP are compared in Figure 8.1, showing excellent agreement between the HD-NNP and direct DFT calculations. The employed computational setup for the DFT calculations is described in Section 7.2. Furthermore, for the neural network, two hidden layers are used, each with 15 nodes. Finally, the training has been carried out using the RuNNer code[47–49] and the MD has been performed with LAMMPS[50, 51].

8.2.2 Molecular Initial Conditions

The initial translational energy distribution of the molecules has been simulated according to experimental molecular beam parameters (stream velocities and width parameters)[9], which are provided in Table 8.1. Experimental beam parameters are available for nozzle temperatures lower than 900 K[9, 10], but here the choice was made to take the width parameter simply as $\alpha = 0.05\nu_0$, which is in reasonable agreement with experiment as can be seen in Figure 8.2a. The width parameters for $T_n = 950$ and 1000 K were obtained by extrapolating the experimental width parameters obtained by Utz and co-workers[9]. Although $\alpha = 0.055\nu_0$ would have been a better approximation for $\nu_0 < 4000$ m/s, this does not have a large effect on the results presented in this work. The stream velocities are obtained by fitting the experimental data using a linear fit (see Figure 8.2b). The exception is the stream velocities for $T_n = 900$ and 1000 K, for which the stream velocities previously used in the BOMD study in Chapter 7 are taken.

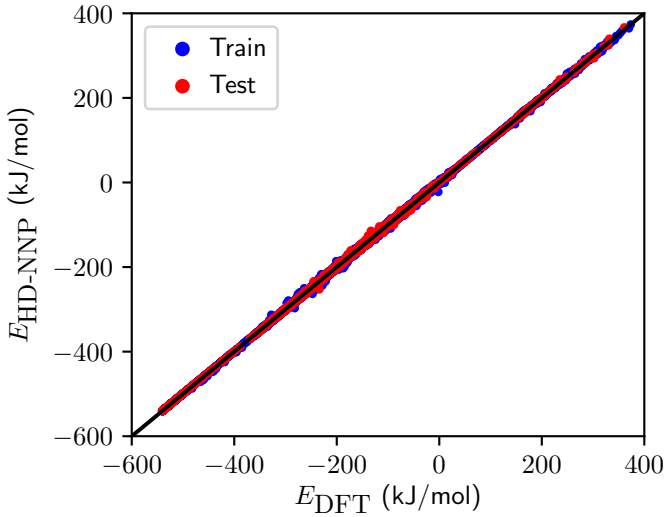

FIGURE 8.1: Total energy for all structures in the training (blue) and testing (red) data set obtained with the HD-NNP and DFT. The total energy of the methane in the gas phase with an ideal surface is taken as zero. The black line indicates $x = y$.

TABLE 8.1: Beam parameters that describe the simulated CHD_3 velocity distributions. ν_0 and α are determined through time-of-flight measurements for 900 K[9]. All other parameters than $\langle E_i \rangle = 160.4$ kJ/mol are not from experiment, but theoretical estimates obtained by interpolation and extrapolation.

T_n (K)	$\langle E_i \rangle$ kJ/mol	ν_0 (m/s)	α (m/s)
400	83.4	2946.95	147.35
500	97.0	3177.70	158.89
600	111.6	3408.45	170.42
700	127.3	3639.20	181.96
800	143.9	3869.95	193.50
900*	160.4	4070.12	274.51
950	172.3	4216.08	300.00
1000	181.3	4320.12	324.01

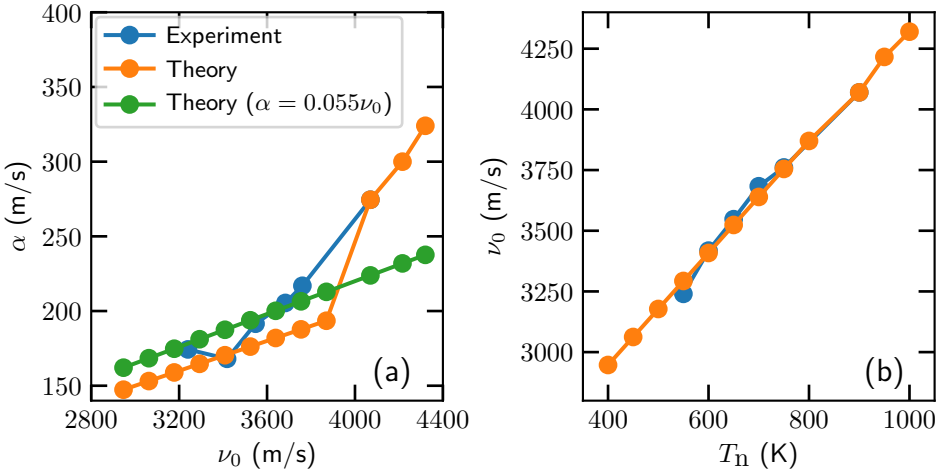

FIGURE 8.2: Width parameter α as a function of the stream velocity ν_0 (a) and the stream velocity ν_0 as a function of the nozzle temperature T_n (b). Experimental parameters[9] and parameters used in this work are indicated in blue and orange, respectively. Theoretical parameters where $\alpha = 0.055\nu_0$ are indicated in green.

8.3 Results

First, the accuracy of the HD-NNP is tested by comparing the 2D elbow plot of methane on Cu(111) in which methane is fixed in all molecular coordinates according to its TS geometry, as depicted in Figure 8.3a, except for Z_C and r (the distance between the carbon atom and surface, and the length of the dissociating CH bond). The HD-NNP is compared directly with DFT calculations in Figure 8.3b. Here, it can be seen that the HD-NNP reproduces the DFT data remarkably well, even though points from the 2D cut are not included in the data set. When the methane is relaxed in all degrees of freedom other than r and Z (Figure 8.3c), the MEP lies slightly closer to the surface than to the MEP of the constrained methane. Again, the HD-NNP reproduces the direct DFT calculations quite well. Moreover, both the electronic and mechanical coupling[30] are in good agreement with DFT (see Figure 8.3d,e), which means that changes in the barrier height and geometry with respect to the motion of the surface atom below the dissociating molecule are described correctly. Furthermore, using 90% of the DFT data set as the training set and 10% as the test set, the RMSE is 1.7 kJ/mol for the test set, which is well within chemical accuracy (4.2 kJ/mol). (Note that all errors reported in this chapter are with respect to the full system, i.e., the total energy.) The high fitting accuracy is

also observed in Figure 8.4, where the distributions of the absolute error for the training and test set are shown and the vast majority of the errors falls within chemical accuracy. The total energy for all of the structures in the training and test set obtained with the HD-NNP and direct DFT calculations is also shown in Figure 8.1. Moreover, the RMSE for the forces in the test set is 2.3 kJ/mol/Å. The RMSE of 1.7 kJ/mol is obtained here on the basis of 38 000 DFT points for CHD_3 + Cu(111), where the surface atoms are allowed to move. This RMSE value compares well with the RMSE of 1.5 kJ/mol obtained for a recent 15D NN static surface PES for CHD_3 + Ni(111), on the basis of 200 000 DFT points[19, 28]. It should also be noted that the approximate modified generalized Langevin oscillator method used in Ref. [28] to effectively add surface atom motion to the MD may run into problems if the molecule-metal surface interaction depends on more than just one surface atom coordinate, as for instance is the case for H_2O + Ni(111)[52], and may be the case for methane interacting with stepped metal surfaces[28].

The goal is to make a HD-NNP with which it is possible to accurately evaluate the energy and forces on the fly during MD simulations. Therefore, not only incidence energies with low reaction probabilities ($< 1\%$) are investigated, but also regimes with higher reaction probabilities that are obtainable with BOMD in order to test the validity of the results obtained with the HD-NNP. Figure 8.5 shows the results obtained for the dissociative chemisorption of CHD_3 on Cu(111) with MD using the HD-NNP and with BOMD[12] (see also Chapter 7 and Table 7.5), by simulating a molecular beam for the rovibrational ground state and under laser-off and laser-on conditions. Under laser-off conditions the molecular beam's vibrational state population is sampled according to the nozzle temperature. We also present results for the case that under laser-on conditions the CH stretch mode ν_1 is excited with one or two quanta. In order to describe the reaction probability with good statistics, 10 000 - 110 000 quasiclassical trajectories were computed per incidence condition. Here, it can be seen that at high incidence energy and for vibrationally excited methane, for four sets of initial conditions resulting in reaction probabilities obtained with BOMD, good agreement exists between BOMD and MD performed with the HD-NNP (see also Table 8.2 and the statistical analysis in Section 8.C). Moreover, reaction probabilities as low as 5×10^{-5} have been computed with the HD-NNP (Figure 8.5), which was previously not possible using accurate methods. It is observed that at the highest incidence energy (181 kJ/mol) the laser-off simulation yields a similar reaction probability as the $\nu_1 = 1$ simulation, which is caused by the high amount of vibrational excitation in the laser-off beam due to the high simulated nozzle temperature ($T_n = 1000$ K). However, it should be noted that sticking probabilities computed for laser-off

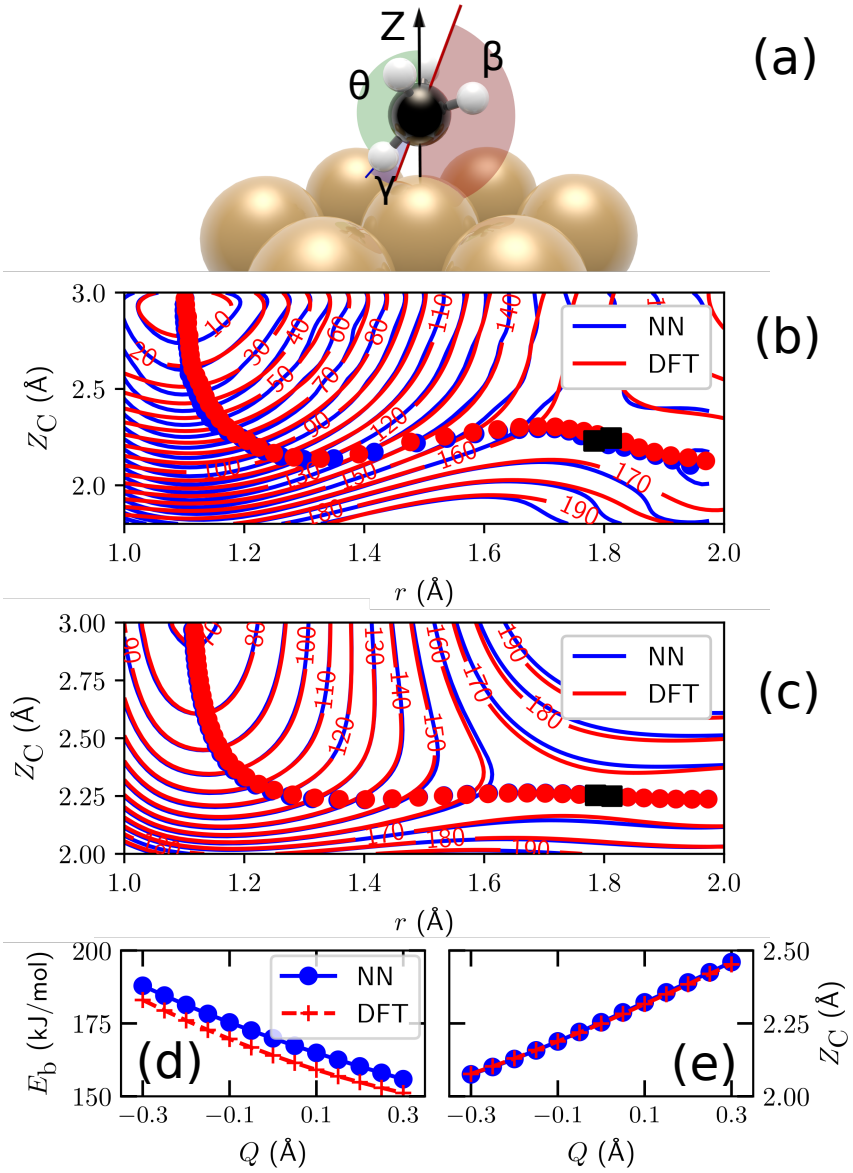

FIGURE 8.3: (a) TS geometry of methane on Cu(111), indicating the θ, β and γ angles (see Section 7.3.1 for further explanation). (b) Elbow plot of methane on Cu(111) as a function of Z_C and r (distance between the carbon atom and surface, and the length of the dissociating CH-bond, respectively), where other degrees of freedom are fixed according to the TS. Contour lines are drawn at intervals of 10 kJ/mol between 0 and 200 kJ/mol. The blue and red lines are NN and DFT results, respectively. The circles indicate the MEP. (c) Same as (b), but with all degrees of freedom of the methane relaxed, except Z_C and r. (d,e) Variation of the height (d) and location (e) of the barrier as a function of the vertical displacement Q of the nearest top layer Cu atom.

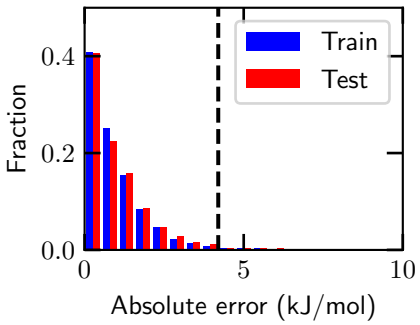

FIGURE 8.4: Distribution of absolute total energy errors (kJ/mol) of the HD-NNP compared to the DFT total energy. Blue indicates the training set, whereas red indicates the test set. The dashed line indicates chemical accuracy, i.e., 4.2 kJ/mol.

TABLE 8.2: Reaction probabilities (P_R) obtained with the HD-NNP and BOMD. The error bars represent 68% confidence intervals.

$\langle E_i \rangle$ (kJ/mol)	Quantum state	P_R (HD-NNP)	P_R (BOMD)
160.4	$\nu_1 = 1$	0.0007 ± 0.0002	0.000 ± 0.001
160.4	$\nu_1 = 2$	0.0246 ± 0.0016	0.024 ± 0.005
181.3	$\nu_1 = 1$	0.0025 ± 0.0005	0.005 ± 0.002
181.3	$\nu_1 = 2$	0.0486 ± 0.0022	0.048 ± 0.007

conditions and nozzle temperatures higher than 650 K may be unreliable due to intramolecular vibrational-energy redistribution among vibrational states in which CD bends and stretches are excited[9].

The dynamical simulations in this chapter show that the reaction of methane is promoted both by translational and vibrational energy. Plotting the reaction probability as a function of the total energy (vibrational + translational energy) shows that putting vibrational energy into the reaction is almost equally or more efficient than increasing the translational energy, depending on the amount of quanta in the ν_1 CH stretch mode (see Figure 8.5b). The vibrational efficacy is equal to or larger than 0.8, which can be expected for such a late barrier system[53] combined with an MEP of the shape shown in Figure 8.3b,c, causing incoming molecules having to react over considerably higher barriers because they run off the MEP ("the bobsled effect"[54, 55]). This could play a large role at catalytic conditions, where graphene is produced from methane using very high temperatures (> 1200 K)[36, 41] and thus vibrational excitation is prevalent. Interestingly, the vibrational efficacy[56, 57] for the excitation from the $\nu_1 = 1$ to $\nu_1 = 2$ overtone ($\eta_{\nu_1=2,1} = 1.7$) is considerably higher than that for the excitation from the ground state to $\nu_1 = 1$ ($\eta_{\nu_1=1,0} = 0.8$). To

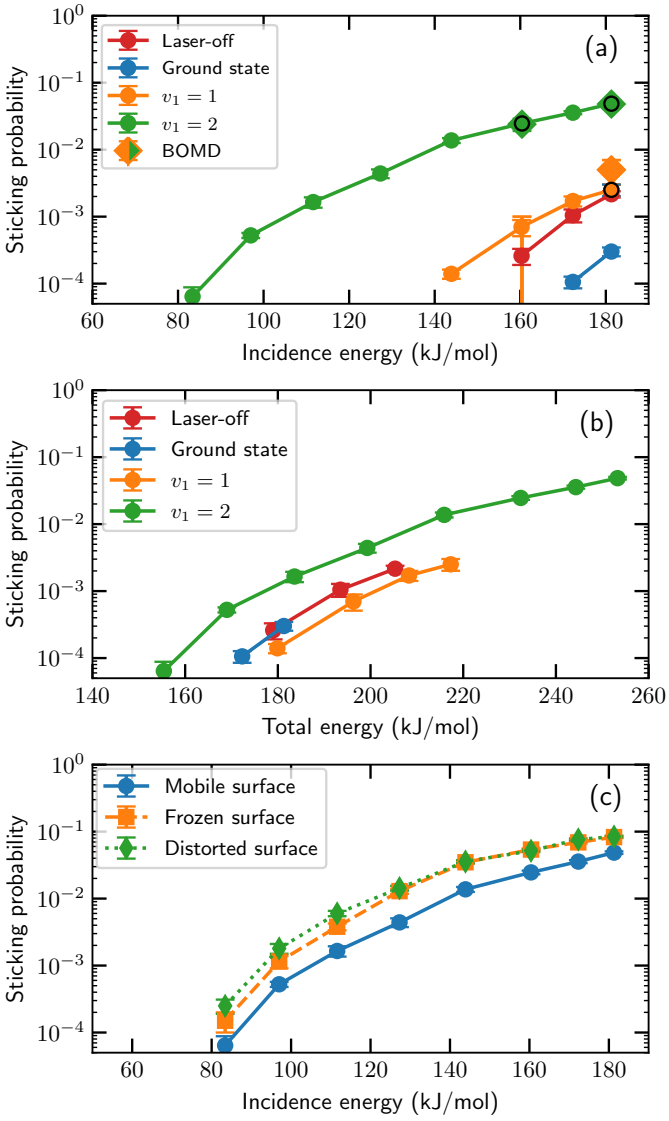

FIGURE 8.5: (a) Initial state-selected and molecular beam sticking probabilities of CHD_3 on Cu(111) as a function of the translational energy for a surface temperature of 550 K. Simulations for laser-off (red), rovibrational ground state (blue), $\nu_1 = 1$ (orange) and $\nu_1 = 2$ (green), where the circles and diamonds are HD-NNP and BOMD results, respectively. (b) Same as panel a, but here the reaction probability is shown as a function of the total energy (vibrational + translational energy). (c) Simulations for $\nu_1 = 2$ with (blue solid line with circles) and without surface motion, where the orange squares with a dashed line indicate an ideal surface and the green diamonds with a dotted line indicate a thermally distorted surface. The error bars represent 68% confidence intervals.

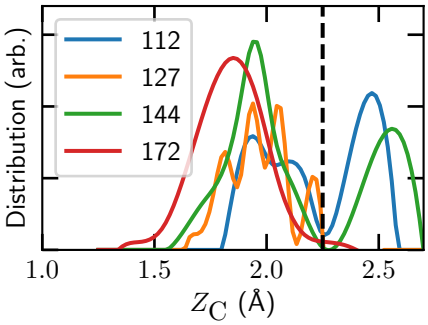

FIGURE 8.6: Distributions of the height of the carbon atom when a CH-bond dissociates (i.e., $r = r^{\ddagger}$) for $\nu_1 = 2$ at various incidence energies (numbers are in kJ/mol). The TS geometry value for Z_C is indicated by the dashed line.

the best of our knowledge, a higher vibrational efficacy for an overtone has not been observed before[56–60]. In Figure 8.6, it is observed that when the incidence energy decreases, for $\nu_1 = 2$, reacted trajectories follow the MEP more closely. Furthermore, an increase of vibrational energy causes reacting trajectories to follow the MEP more closely as well (see Figure 8.7a). The dynamical effect (see Figure 8.7b) is that, because a higher incidence energy is needed to overcome the barrier for a low ν_1, for low ν_1 the carbon atom smashes into the repulsive wall. The hydrogen atom moves out while the carbon atom is still close to the surface, and therefore a higher barrier needs to be overcome (see Figure 8.7). Hence, a higher vibrational efficacy is observed for $\nu_1 = 2$ since the bobsled effect will be less prominent and thus lower barriers need to be overcome.

It has been already noted that the reaction probabilities at high incidence energy obtained with the HD-NNP are in good agreement with BOMD. However, the validity of the quasi-classical approximation for the low reaction probabilities needs to be tested by comparison to experiment due to the possibility of quantum effects, and potential problems with zero-point energy violation, even though it has been shown that at elevated surface temperature the reaction of methane happens in a "classical over the barrier fashion" with assistance of surface atom motion and without the need for tunneling[4, 61].

The main goal of applying the Behler-Parrinello method to polyatomic molecules is to be able to include explicitly surface motion. Therefore, to evaluate the effect of surface motion, reaction probabilities for $\nu_1 = 2$ have also been computed using a static surface model, where the surface was kept in its ideal relaxed static configuration (note that the lattice expansion corresponding to a surface temperature of 550 K was kept). This effectively removes energy transfer between the molecule and the surface and the corrugation in barrier heights and positions related to surface motion. Reaction probabilities for this

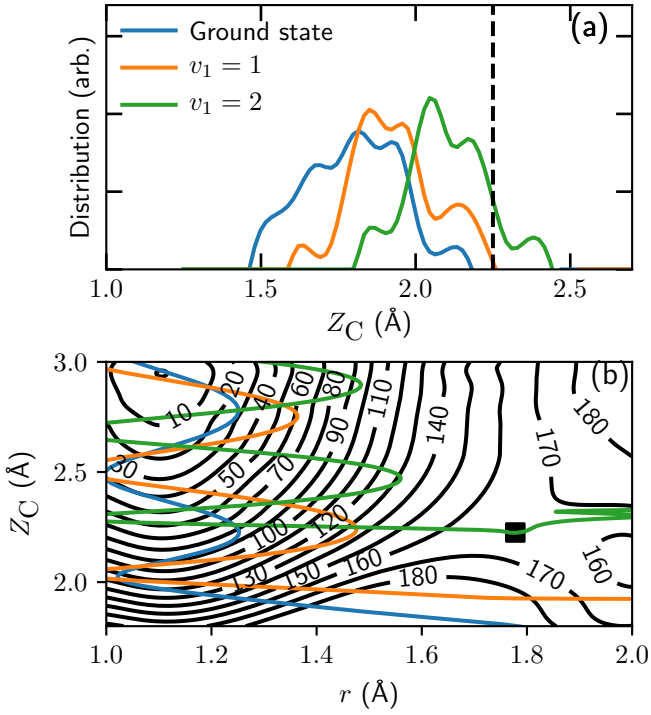

FIGURE 8.7: (a) Distributions of the height of the carbon (Z_C) when a CH bond dissociates, i.e., $r = r^{\ddagger}$, for the rovibrational ground state, $v_1 = 1$, and $v_1 = 2$ at incidence energies with comparable reaction probabilities (about 0.03%). The TS geometry value for Z_C is indicated by the dashed line. (b) Elbow plot of methane on Cu(111) obtained with the HD-NNP, where Z_C and r (distance between the carbon atom and surface, and the length of the dissociating CH-bond, respectively) are variable and all other degrees of freedom are relaxed. Contour lines are drawn at intervals of 10 kJ/mol between 0 and 180 kJ/mol. Typical trajectories that go on to react for $P = 0.03\%$ are indicated by the blue (ground state), orange ($v_1 = 1$) and green ($v_1 = 2$) lines. The black square indicates the highest point along the MEP.

frozen surface are a factor 2 higher than those when surface motion is allowed (see Figure 8.5c). Furthermore, when the distortions of a hot surface are included while still excluding surface motion, i.e., modeling a static thermally disordered surface (similar to the so-called static corrugation model[62]), reaction probabilities are increased by 50% compared to the frozen ideal surface at low incidence energies. At high incidence energies, no difference is observed between the results for the static ideal and the distorted surface, with the latter including the effect of the electronic coupling (or the so-called β-coupling)[30]. The observation that explicitly including surface motion at these high incidence energies lowers the reaction probabilities suggests that the reaction probabilities are decreased due to energy transfer to the surface atoms as the molecule first impacts on the surface (Figure 8.7b) and possibly also due to surface recoil (mechanical coupling)[4, 30]. Because the surface recoil effect (which is due to surface atom vibrational averaging) tends to be small[30], it is suspected that the energy transfer is most important. This effect can only be addressed with explicit modeling of the surface motion and not by the sudden and energy averaging methods typically used with quantum dynamics simulations[30].

8.4 Conclusions

In this chapter the Behler-Parrinello approach is used to develop an HD-NNP that describes a polyatomic molecule reacting on a mobile metal surface, i.e., CHD_3 + Cu(111). The HD-NNP is found to be in good agreement with DFT, which means that MD can be performed with the accuracy of BOMD but with a considerably lower computational effort. Using this HD-NNP, reaction probabilities as low as 5×10^{-5} have been obtained, which are untractable with previous accurate methods such as BOMD, while including surface motion. It is found that vibrational excitation plays a major role in the reactivity, where the overtone has a higher vibrational efficacy than the fundamental vibrational excitation. Moreover, allowing energy transfer from the molecule to the surface atoms considerably reduces the overall reactivity. Hence, surface motion needs to be included explicitly in simulations in order to obtain quantitative results for molecular beam simulations of methane reacting on copper. More work is still required to investigate the effect of surface temperature on the reaction of CHD_3 on Cu(111), since only one surface temperature (550 K) is addressed. Finally, the quasi-classical approximation needs to be tested for low reaction probabilities by comparison to experiments due to the possibility of quantum effects and zero-point energy violation. However, this would not

be an intrinsic problem of the HD-NNP as good agreement with DFT has been shown.

Appendix

8.A Symmetry Functions

The parameters used for the radial and angular symmetry functions are given in Tables 8.A.1 and 8.A.2, and the cut-off radius $R_c = 13\,a_0$. Note that $\eta = 0$ for all angular symmetry functions.

8.B Elbow Plots

Due to the difficulty of relaxing the methane geometry in 13 degrees of freedom, a smoothing function was used for the elbow plot in Figure 8.3c and 8.7b. Figure 8.B.1 shows the elbow plot obtained with the HD-NNP in Figure 8.3c without smoothing, where the HD-NNP and direct DFT calculations are still in good agreement.

Furthermore, Figure 8.B.2 shows the elbow plots for methane on Cu(111) and Ni(111)[9]. The obtained MEPs seem very similar, where the main difference is that on Ni(111) the barrier is earlier and the barrier height is lower than on Cu(111). However, when the energy along the MEP is taken into account as well (see Figure 8.B.3), it is observed that the MEP of Cu(111) is much more repulsive. Therefore, methane needs a considerably higher energy in order to overcome the barrier, causing trajectories in general to experience the bobsled effect.

8.C Statistical Analysis

A statistical analysis is performed in order to see whether the HD-NNP and BOMD reaction probabilities are in agreement. Fischer's exact test[63] is used to evaluate a null hypothesis, which is defined here as $P_{\text{HD-NNP}} = P_{\text{BOMD}}$. The results obtained both with the HD-NNP and BOMD using a significance level of $\alpha = 0.05$ are in agreement, hence, the conclusion is that the reaction probabilities obtained with the HD-NNP and BOMD are in agreement.

TABLE 8.A.1: Parameters used for the radial symmetry functions (see Eq. 2.38) describing the interaction of the reference atom (Ref.) with its neighbouring atoms (Neighb.) within the cut-off radius.

Ref.	Neighb.	η	Ref.	Neighb.	η	Ref.	Neighb.	η
H	C	0	Cu	C	0	C	H	0
H	C	0.007	Cu	C	0.007	C	H	0.007
H	C	0.018	Cu	C	0.018	C	H	0.018
H	C	0.036	Cu	C	0.035	C	H	0.036
H	C	0.068	Cu	C	0.065	C	H	0.068
H	C	0.13	Cu	C	0.12	C	H	0.13
H	C	0.27	Cu	C	0.24	C	H	0.27
H	C	0.7	Cu	C	0.55	C	H	0.7
H	H	0	Cu	H	0	C	Cu	0
H	H	0.007	Cu	H	0.007	C	Cu	0.007
H	H	0.018	Cu	H	0.018	C	Cu	0.018
H	H	0.035	Cu	H	0.035	C	Cu	0.035
H	H	0.065	Cu	H	0.068	C	Cu	0.065
H	H	0.12	Cu	H	0.13	C	Cu	0.12
H	H	0.24	Cu	H	0.27	C	Cu	0.24
H	H	0.55	Cu	H	0.7	C	Cu	0.55
H	Cu	0	Cu	Cu	0			
H	Cu	0.007	Cu	Cu	0.007			
H	Cu	0.018	Cu	Cu	0.018			
H	Cu	0.035	Cu	Cu	0.035			
H	Cu	0.068	Cu	Cu	0.065			
H	Cu	0.13	Cu	Cu	0.12			
H	Cu	0.27	Cu	Cu	0.24			
H	Cu	0.7	Cu	Cu	0.55			

TABLE 8.A.2: Parameters used for the angular symmetry functions (see Eq. 2.39) describing the interaction of the reference atom (Ref.) with its neighbouring atoms (Neighb. 1 and 2) within the cut-off radius.

Ref.	Neighb. 1	Neighb. 2	λ	ζ	Ref.	Neighb. 1	Neighb. 2	λ	ζ	Ref.	Neighb. 1	Neighb. 2	λ	ζ
H	H	H	1	5	Cu	Cu	Cu	1	1					
H	H	H	1	7.5	Cu	Cu	Cu	1	1.7					
H	H	H	1	12	Cu	Cu	Cu	1	3					
H	H	H	1	20	Cu	Cu	Cu	1	6					
H	H	H	1	40	Cu	Cu	Cu	1	15					
					Cu	Cu	Cu	1	68					
H	H	H	-1	1.3	Cu	Cu	Cu	-1	1					
H	H	H	-1	1.9	Cu	Cu	Cu	-1	1.7					
H	H	H	-1	2.8	Cu	Cu	Cu	-1	3					
H	H	H	-1	4.3	Cu	Cu	Cu	-1	6					
H	H	H	-1	7	Cu	Cu	Cu	-1	15					
H	H	C	1	9	Cu	Cu	C	1	1					
H	H	C	1	13	Cu	Cu	C	1	1.7					
H	H	C	1	21	Cu	Cu	C	1	3					
H	H	C	1	38	Cu	Cu	C	1	6					
H	H	C	1	80	Cu	Cu	C	1	15					
					Cu	Cu	C	1	68					
H	H	C	-1	1	Cu	Cu	C	-1	1					
H	H	C	-1	1.3	Cu	Cu	C	-1	1.7					
H	H	C	-1	1.8	Cu	Cu	C	-1	3					
H	H	C	-1	2.5	Cu	Cu	C	-1	6					
H	H	C	-1	3.5	Cu	Cu	C	-1	15					
H	Cu	H	1	1	Cu	H	H	1	1	C	H	H	1	1.2
H	Cu	H	1	1.7	Cu	H	H	1	1.7	C	H	H	1	1.8
H	Cu	H	1	3	Cu	H	H	1	3	C	H	H	1	3
H	Cu	H	1	6	Cu	H	H	1	6	C	H	H	1	5.3
H	Cu	H	1	15	Cu	H	H	1	15	C	H	H	1	10
H	Cu	H	1	68	Cu	H	H	1	68					
H	Cu	H	-1	1	Cu	H	H	-1	1	C	H	H	-1	5
H	Cu	H	-1	1.7	Cu	H	H	-1	1.27	C	H	H	-1	8
H	Cu	H	-1	3	Cu	H	H	-1	1.65	C	H	H	-1	13
H	Cu	H	-1	6	Cu	H	H	-1	2.15	C	H	H	-1	23
H	Cu	H	-1	15	Cu	H	H	-1	2.9	C	H	H	-1	50
H	Cu	H	-1	68	Cu	H	H	-1	4					
H	Cu	C	1	1	Cu	H	C	1	1	C	H	Cu	1	1
H	Cu	C	1	1.7	Cu	H	C	1	1.7	C	H	Cu	1	1.7
H	Cu	C	1	3	Cu	H	C	1	3	C	H	Cu	1	3
H	Cu	C	1	6	Cu	H	C	1	6	C	H	Cu	1	6
H	Cu	C	1	15	Cu	H	C	1	15	C	H	Cu	1	15
H	Cu	C	1	68	Cu	H	C	1	68	C	H	Cu	1	68
H	Cu	C	-1	1	Cu	H	C	-1	1	C	H	Cu	-1	1
H	Cu	C	-1	1.27	Cu	H	C	-1	1.27	C	H	Cu	-1	1.27
H	Cu	C	-1	1.65	Cu	H	C	-1	1.65	C	H	Cu	-1	1.65
H	Cu	C	-1	2.15	Cu	H	C	-1	2.15	C	H	Cu	-1	2.15
H	Cu	C	-1	2.9	Cu	H	C	-1	2.9	C	H	Cu	-1	2.9
H	Cu	C	-1	4	Cu	H	C	-1	4	C	H	Cu	-1	4
H	Cu	Cu	1	1	Cu	Cu	H	1	1	C	Cu	Cu	1	1
H	Cu	Cu	1	1.7	Cu	Cu	H	1	1.7	C	Cu	Cu	1	1.7
H	Cu	Cu	1	3	Cu	Cu	H	1	3	C	Cu	Cu	1	3
H	Cu	Cu	1	6	Cu	Cu	H	1	6	C	Cu	Cu	1	6
H	Cu	Cu	1	15	Cu	Cu	H	1	15	C	Cu	Cu	1	15
H	Cu	Cu	1	68	Cu	Cu	H	1	68	C	Cu	Cu	1	68
H	Cu	Cu	-1	1	Cu	Cu	H	-1	1	C	Cu	Cu	-1	1
H	Cu	Cu	-1	1.27	Cu	Cu	H	-1	1.7	C	Cu	Cu	-1	1.27
H	Cu	Cu	-1	1.65	Cu	Cu	H	-1	3	C	Cu	Cu	-1	1.65
H	Cu	Cu	-1	2.15	Cu	Cu	H	-1	6	C	Cu	Cu	-1	2.15
H	Cu	Cu	-1	2.9	Cu	Cu	H	-1	15	C	Cu	Cu	-1	2.9
H	Cu	Cu	-1	4	Cu	Cu	H	-1	68	C	Cu	Cu	-1	4

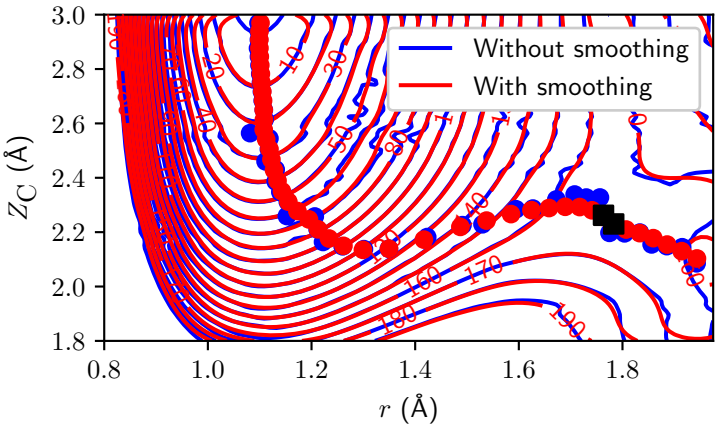

FIGURE 8.B.1: Elbow plot of methane on Cu(111) obtained with the HD-NNP with (red) and without (blue) smoothing, where Z_C and r (distance between the carbon atom and surface, and the length of the dissociating CH bond, respectively) are variable. Contour lines are drawn at intervals of 10 kJ/mol between 0 and 200 kJ/mol. The circles indicate the MEP and the black squares indicate the highest point along the MEPs.

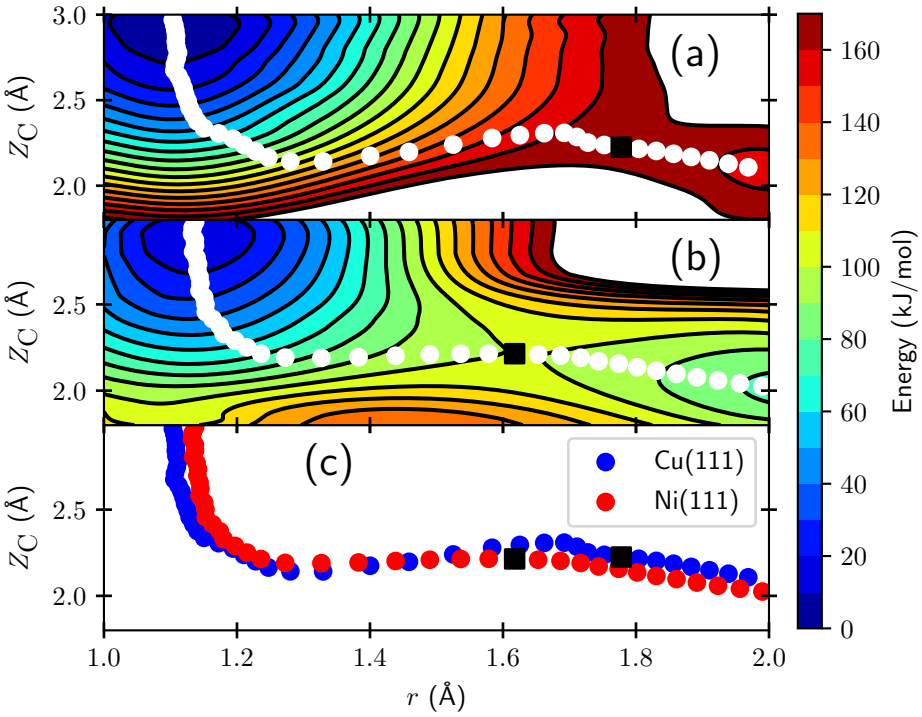

FIGURE 8.B.2: (a) Elbow plot of methane on Cu(111) obtained with the HD-NNP, where Z and r (distance between the carbon atom and surface, and the length of the dissociating CH bond, respectively) are variable and all other degrees of freedom are relaxed. Contour lines are drawn at intervals of 10 kJ/mol between 0 and 180 kJ/mol. The white circles indicate the MEP and the black square indicates the highest point along the MEP. (b) Same as (a) but for methane on Ni(111)[9]. (c) The MEPs for (a) (blue) and (b) (red).

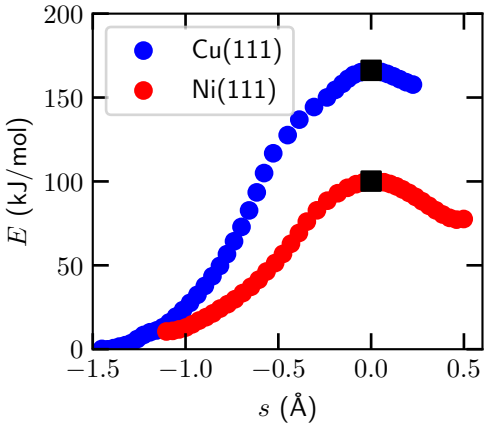

FIGURE 8.B.3: Minimum energy path of methane on Cu(111) (blue) and Ni(111) (red) as a function of the reaction coordinate s. The black squares indicate indicate the highest points along the MEPs.

References

(1) Ertl, G. Primary Steps in Catalytic Synthesis of Ammonia. *J. Vac. Sci. Technol. A* **1983**, *1*, 1247–1253, DOI: 10.1116/1.572299.

(2) Wei, J.; Iglesia, E. Mechanism and Site Requirements for Activation and Chemical Conversion of Methane on Supported Pt Clusters and Turnover Rate Comparisons among Noble Metals. *J. Phys. Chem. B* **2004**, *108*, 4094–4103, DOI: 10.1021/jp036985z.

(3) Kroes, G.-J. Towards Chemically Accurate Simulation of Molecule–Surface Reactions. *Phys. Chem. Chem. Phys.* **2012**, *14*, 14966–14981, DOI: 10.1039/C2CP42471A.

(4) Jackson, B.; Nattino, F.; Kroes, G.-J. Dissociative Chemisorption of Methane on Metal Surfaces: Tests of Dynamical Assumptions Using Quantum Models and Ab Initio Molecular Dynamics. *J. Chem. Phys.* **2014**, *141*, 054102, DOI: 10.1063/1.4891327.

(5) Wellendorff, J.; Silbaugh, T. L.; Garcia-Pintos, D.; Nørskov, J. K.; Bligaard, T.; Studt, F.; Campbell, C. T. A Benchmark Database for Adsorption Bond Energies to Transition Metal Surfaces and Comparison to Selected DFT Functionals. *Surf. Sci.* **2015**, *640*, 36–44, DOI: 10.1016/j.susc.2015.03.023.

(6) Gautier, S.; Steinmann, S. N.; Michel, C.; Fleurat-Lessard, P.; Sautet, P. Molecular Adsorption at Pt(111). How Accurate Are DFT Functionals? *Phys. Chem. Chem. Phys.* **2015**, *17*, 28921–28930, DOI: 10.1039/C5CP04534G.

(7) Kroes, G.-J. Toward a Database of Chemically Accurate Barrier Heights for Reactions of Molecules with Metal Surfaces. *J. Phys. Chem. Lett.* **2015**, *6*, 4106–4114, DOI: 10.1021/acs.jpclett.5b01344.

(8) Füchsel, G.; Zhou, X.; Jiang, B.; Juaristi, J. I.; Alducin, M.; Guo, H.; Kroes, G.-J. Reactive and Nonreactive Scattering of HCl from Au(111): An Ab Initio Molecular Dynamics Study. *J. Phys. Chem. C* **2019**, *123*, 2287–2299, DOI: 10.1021/acs.jpcc.8b10686.

(9) Nattino, F.; Migliorini, D.; Kroes, G.-J.; Dombrowski, E.; High, E. A.; Killelea, D. R.; Utz, A. L. Chemically Accurate Simulation of a Polyatomic Molecule-Metal Surface Reaction. *J. Phys. Chem. Lett.* **2016**, *7*, 2402–2406, DOI: 10.1021/acs.jpclett.6b01022.

(10) Migliorini, D.; Chadwick, H.; Nattino, F.; Gutiérrez-González, A.; Dombrowski, E.; High, E. A.; Guo, H.; Utz, A. L.; Jackson, B.; Beck, R. D.; Kroes, G.-J. Surface Reaction Barriometry: Methane Dissociation on Flat and Stepped Transition-Metal Surfaces. *J. Phys. Chem. Lett.* **2017**, *8*, 4177–4182, DOI: 10.1021/acs.jpclett.7b01905.

(11) Chadwick, H.; Gutiérrez-González, A.; Migliorini, D.; Beck, R. D.; Kroes, G.-J. Incident Angle Dependence of CHD_3 Dissociation on the Stepped Pt(211) Surface. *J. Phys. Chem. C* **2018**, *122*, 19652–19660, DOI: 10.1021/acs.jpcc.8b05887.

(12) Gerrits, N.; Migliorini, D.; Kroes, G.-J. Dissociation of CHD_3 on Cu(111), Cu(211), and Single Atom Alloys of Cu(111). *J. Chem. Phys.* **2018**, *149*, 224701, DOI: 10.1063/1.5053990.

(13) Shakouri, K.; Behler, J.; Meyer, J.; Kroes, G.-J. Accurate Neural Network Description of Surface Phonons in Reactive Gas–Surface Dynamics: N_2 + Ru(0001). *J. Phys. Chem. Lett.* **2017**, *8*, 2131–2136, DOI: 10.1021/acs.jpclett.7b00784.

(14) Kolb, B.; Luo, X.; Zhou, X.; Jiang, B.; Guo, H. High-Dimensional Atomistic Neural Network Potentials for Molecule–Surface Interactions: HCl Scattering from Au(111). *J. Phys. Chem. Lett.* **2017**, *8*, 666–672, DOI: 10.1021/acs.jpclett.6b02994.

(15) Shakouri, K.; Behler, J.; Meyer, J.; Kroes, G.-J. Analysis of Energy Dissipation Channels in a Benchmark System of Activated Dissociation: N_2 on Ru(0001). *J. Phys. Chem. C* **2018**, *122*, 23470–23480, DOI: 10.1021/acs.jpcc.8b06729.

(16) Liu, Q.; Zhou, X.; Zhou, L.; Zhang, Y.; Luo, X.; Guo, H.; Jiang, B. Constructing High-Dimensional Neural Network Potential Energy Surfaces for Gas–Surface Scattering and Reactions. *J. Phys. Chem. C* **2018**, *122*, 1761–1769, DOI: 10.1021/acs.jpcc.7b12064.

(17) Jiang, B.; Guo, H. Dynamics of Water Dissociative Chemisorption on Ni(111): Effects of Impact Sites and Incident Angles. *Phys. Rev. Lett.* **2015**, *114*, 166101, DOI: 10.1103/PhysRevLett.114.166101.

(18) Shen, X.; Chen, J.; Zhang, Z.; Shao, K.; Zhang, D. H. Methane Dissociation on Ni(111): A Fifteen-Dimensional Potential Energy Surface Using Neural Network Method. *J. Chem. Phys.* **2015**, *143*, 144701, DOI: 10.1063/1.4932226.

(19) Zhou, X.; Nattino, F.; Zhang, Y.; Chen, J.; Kroes, G.-J.; Guo, H.; Jiang, B. Dissociative Chemisorption of Methane on Ni(111) Using a Chemically Accurate Fifteen Dimensional Potential Energy Surface. *Phys. Chem. Chem. Phys.* **2017**, *19*, 30540–30550, DOI: 10.1039/C7CP05993K.

(20) Hu, X.; Yang, M.; Xie, D.; Guo, H. Vibrational Enhancement in the Dynamics of Ammonia Dissociative Chemisorption on Ru(0001). *J. Chem. Phys.* **2018**, *149*, 044703, DOI: 10.1063/1.5043517.

(21) Chen, J.; Zhou, X.; Zhang, Y.; Jiang, B. Vibrational Control of Selective Bond Cleavage in Dissociative Chemisorption of Methanol on Cu(111). *Nat. Commun.* **2018**, *9*, 4039, DOI: 10.1038/s41467-018-06478-6.

(22) Zhang, Y.; Zhou, X.; Jiang, B. Bridging the Gap between Direct Dynamics and Globally Accurate Reactive Potential Energy Surfaces Using Neural Networks. *J. Phys. Chem. Lett.* **2019**, *10*, 1185–1191, DOI: 10.1021/acs.jpclett.9b00085.

(23) Tiwari, A. K.; Nave, S.; Jackson, B. The Temperature Dependence of Methane Dissociation on Ni(111) and Pt(111): Mixed Quantum-Classical Studies of the Lattice Response. *J. Chem. Phys.* **2010**, *132*, 134702, DOI: 10.1063/1.3357415.

(24) Nattino, F.; Díaz, C.; Jackson, B.; Kroes, G.-J. Effect of Surface Motion on the Rotational Quadrupole Alignment Parameter of D_2 Reacting on Cu(111). *Phys. Rev. Lett.* **2012**, *108*, 236104, DOI: 10.1103/PhysRevLett.108.236104.

(25) Mondal, A.; Wijzenbroek, M.; Bonfanti, M.; Díaz, C.; Kroes, G.-J. Thermal Lattice Expansion Effect on Reactive Scattering of H_2 from Cu(111) at T_s = 925 K. *J. Phys. Chem. A* **2013**, *117*, 8770–8781, DOI: 10.1021/jp4042183.

(26) Füchsel, G.; del Cueto, M.; Díaz, C.; Kroes, G.-J. Enigmatic HCl + Au(111) Reaction: A Puzzle for Theory and Experiment. *J. Phys. Chem. C* **2016**, *120*, 25760–25779, DOI: 10.1021/acs.jpcc.6b07453.

(27) Gerrits, N.; Kroes, G.-J. An AIMD Study of Dissociative Chemisorption of Methanol on Cu(111) with Implications for Formaldehyde Formation. *J. Chem. Phys.* **2019**, *150*, 024706, DOI: 10.1063/1.5070129.

(28) Zhou, X.; Jiang, B. A Modified Generalized Langevin Oscillator Model for Activated Gas-Surface Reactions. *J. Chem. Phys.* **2019**, *150*, 024704, DOI: 10.1063/1.5078541.

(29) Baule, B. Theoretische Behandlung Der Erscheinungen in Verdünnten Gasen. *Ann. Phys.* **1914**, *349*, 145–176, DOI: 10.1002/andp.19143490908.

(30) Guo, H.; Farjamnia, A.; Jackson, B. Effects of Lattice Motion on Dissociative Chemisorption: Toward a Rigorous Comparison of Theory with Molecular Beam Experiments. *J. Phys. Chem. Lett.* **2016**, *7*, 4576–4584, DOI: 10.1021/acs.jpclett.6b01948.

(31) Frankcombe, T. J. Interpolating DFT Data for 15D Modeling of Methane Dissociation on an Fcc Metal. *Int. J. Chem. Kinet.* **2018**, *50*, 285–293, DOI: 10.1002/kin.21157.

(32) Shen, X. J.; Lozano, A.; Dong, W.; Busnengo, H. F.; Yan, X. H. Towards Bond Selective Chemistry from First Principles: Methane on Metal Surfaces. *Phys. Rev. Lett.* **2014**, *112*, 046101, DOI: 10.1103/PhysRevLett.112.046101.

(33) Lozano, A.; Shen, X. J.; Moiraghi, R.; Dong, W.; Busnengo, H. F. Cutting a Chemical Bond with Demon's Scissors: Mode- and Bond-Selective Reactivity of Methane on Metal Surfaces. *Surf. Sci.* **2015**, *640*, 25–35, DOI: 10.1016/j.susc.2015.04.002.

(34) Seminara, G. N.; Peludhero, I. F.; Dong, W.; Martínez, A. E.; Busnengo, H. F. Molecular Dynamics Study of Molecular and Dissociative Adsorption Using System-Specific Force Fields Based on Ab Initio Calculations: CO/Cu(110) and $$\text {CH_4/\text {Pt(110)$$CH4/Pt(110). *Top. Catal.* **2019**, *62*, 1044–1052, DOI: 10.1007/s11244-019-01196-9.

(35) Moiraghi, R.; Lozano, A.; Peterson, E.; Utz, A.; Dong, W.; Busnengo, H. F. Nonthermalized Precursor-Mediated Dissociative Chemisorption at High Catalysis Temperatures. *J. Phys. Chem. Lett.* **2020**, *11*, 2211–2218, DOI: 10.1021/acs.jpclett.0c00260.

(36) Li, X.; Cai, W.; An, J.; Kim, S.; Nah, J.; Yang, D.; Piner, R.; Velamakanni, A.; Jung, I.; Tutuc, E.; Banerjee, S. K.; Colombo, L.; Ruoff, R. S. Large-Area Synthesis of High-Quality and Uniform Graphene Films on Copper Foils. *Science* **2009**, *324*, 1312–1314, DOI: 10.1126/science.1171245.

(37) Losurdo, M.; Giangregorio, M. M.; Capezzuto, P.; Bruno, G. Graphene CVD Growth on Copper and Nickel: Role of Hydrogen in Kinetics and Structure. *Phys. Chem. Chem. Phys.* **2011**, *13*, 20836–20843, DOI: 10.1039/C1CP22347J.

(38) Zhang, W.; Wu, P.; Li, Z.; Yang, J. First-Principles Thermodynamics of Graphene Growth on Cu Surfaces. *J. Phys. Chem. C* **2011**, *115*, 17782–17787, DOI: 10.1021/jp2006827.

(39) Li, K.; He, C.; Jiao, M.; Wang, Y.; Wu, Z. A First-Principles Study on the Role of Hydrogen in Early Stage of Graphene Growth during the CH_4 Dissociation on Cu(111) and Ni(111) Surfaces. *Carbon* **2014**, *74*, 255–265, DOI: 10.1016/j.carbon.2014.03.030.

(40) Wang, X.; Yuan, Q.; Li, J.; Ding, F. The Transition Metal Surface Dependent Methane Decomposition in Graphene Chemical Vapor Deposition Growth. *Nanoscale* **2017**, *9*, 11584–11589, DOI: 10.1039/C7NR02743E.

(41) Kraus, J.; Böbel, L.; Zwaschka, G.; Günther, S. Understanding the Reaction Kinetics to Optimize Graphene Growth on Cu by Chemical Vapor Deposition. *Ann. Phys.* **2017**, *529*, 1700029, DOI: 10.1002/andp.201700029.

(42) Tian, B.; Liu, T.; Yang, Y.; Li, K.; Wu, Z.; Wang, Y. CH_4 Dissociation in the Early Stage of Graphene Growth on Fe–Cu(100) Surface: Theoretical Insights. *Appl. Surf. Sci.* **2018**, *427*, 953–960, DOI: 10.1016/j.apsusc.2017.09.088.

(43) Rettner, C. T.; Auerbach, D. J.; Lee, J. Dynamics of the Formation of CD_4 from the Direct Reaction of Incident D Atoms with CD_3/Cu(111). *J. Chem. Phys.* **1996**, *105*, 10115–10122, DOI: 10.1063/1.472840.

(44) Behler, J.; Parrinello, M. Generalized Neural-Network Representation of High-Dimensional Potential-Energy Surfaces. *Phys. Rev. Lett.* **2007**, *98*, 146401, DOI: 10.1103/PhysRevLett.98.146401.

(45) Behler, J. Representing Potential Energy Surfaces by High-Dimensional Neural Network Potentials. *J. Phys.: Condens. Matter* **2014**, *26*, 183001, DOI: 10.1088/0953-8984/26/18/183001.

(46) Behler, J. Atom-Centered Symmetry Functions for Constructing High-Dimensional Neural Network Potentials. *J. Chem. Phys.* **2011**, *134*, 074106, DOI: 10.1063/1.3553717.

(47) Behler, J. Constructing High-Dimensional Neural Network Potentials: A Tutorial Review. *Int. J. Quantum Chem.* **2015**, *115*, 1032–1050, DOI: 10.1002/qua.24890.

(48) Behler, J. First Principles Neural Network Potentials for Reactive Simulations of Large Molecular and Condensed Systems. *Angew. Chem. Int. Ed.* **2017**, *56*, 12828–12840, DOI: 10.1002/anie.201703114.

(49) Behler, J. RuNNer - A Neural Network Code for High-Dimensional Neural Network Potential-Energy Surfaces; Universität Göttingen http://www.uni-goettingen.de/de/560580.html (accessed 02/14/2019).

(50) Plimpton, S. Fast Parallel Algorithms for Short-Range Molecular Dynamics. *J. Comput. Phys.* **1995**, *117*, 1–19, DOI: 10.1006/jcph.1995.1039.

(51) Singraber, A.; Behler, J.; Dellago, C. Library-Based LAMMPS Implementation of High-Dimensional Neural Network Potentials. *J. Chem. Theory Comput.* **2019**, *15*, 1827–1840, DOI: 10.1021/acs.jctc.8b00770.

(52) Hundt, P. M.; Jiang, B.; van Reijzen, M. E.; Guo, H.; Beck, R. D. Vibrationally Promoted Dissociation of Water on Ni(111). *Science* **2014**, *344*, 504–507, DOI: 10.1126/science.1251277.

(53) Polanyi, J. C. Concepts in Reaction Dynamics. *Acc. Chem. Res.* **1972**, *5*, 161–168, DOI: 10.1021/ar50053a001.

(54) Marcus, R. A. On the Analytical Mechanics of Chemical Reactions. Quantum Mechanics of Linear Collisions. *J. Chem. Phys.* **1966**, *45*, 4493–4499, DOI: 10.1063/1.1727528.

(55) McCullough, E. A.; Wyatt, R. E. Quantum Dynamics of the Collinear (H, H_2) Reaction. *J. Chem. Phys.* **1969**, *51*, 1253–1254, DOI: 10.1063/1.1672133.

(56) Jiang, B.; Yang, M.; Xie, D.; Guo, H. Quantum Dynamics of Polyatomic Dissociative Chemisorption on Transition Metal Surfaces: Mode Specificity and Bond Selectivity. *Chem. Soc. Rev.* **2016**, *45*, 3621–3640, DOI: 10.1039/C5CS00360A.

(57) Juurlink, L. B. F.; Killelea, D. R.; Utz, A. L. State-Resolved Probes of Methane Dissociation Dynamics. *Prog. Surf. Sci.* **2009**, *84*, 69–134, DOI: 10.1016/j.progsurf.2009.01.001.

(58) Schmid, M. P.; Maroni, P.; Beck, R. D.; Rizzo, T. R. Surface Reactivity of Highly Vibrationally Excited Molecules Prepared by Pulsed Laser Excitation: CH_4 ($2\nu_3$) on Ni(100). *J. Chem. Phys.* **2002**, *117*, 8603–8606, DOI: 10.1063/1.1519860.

(59) Guo, H.; Jackson, B. Mode-Selective Chemistry on Metal Surfaces: The Dissociative Chemisorption of CH_4 on Pt(111). *J. Chem. Phys.* **2016**, *144*, 184709, DOI: 10.1063/1.4948941.

(60) Farjamnia, A.; Jackson, B. The Dissociative Chemisorption of Water on Ni(111): Mode- and Bond-Selective Chemistry on Metal Surfaces. *J. Chem. Phys.* **2015**, *142*, 234705, DOI: 10.1063/1.4922625.

(61) Campbell, V. L.; Chen, N.; Guo, H.; Jackson, B.; Utz, A. L. Substrate Vibrations as Promoters of Chemical Reactivity on Metal Surfaces. *J. Phys. Chem. A* **2015**, *119*, 12434–12441, DOI: 10.1021/acs.jpca.5b07873.

(62) Spiering, P.; Wijzenbroek, M.; Somers, M. F. An Improved Static Corrugation Model. *J. Chem. Phys.* **2018**, *149*, 234702, DOI: 10.1063/1.5058271.

(63) Fisher, R. A. On the Interpretation of X^2 from Contingency Tables, and the Calculation of P. *J. R. Stat. Soc.* **1922**, *85*, 87–94, DOI: 10.2307/2340521.